Published in final edited form as:
Nat Phys. 2021 September ; 17(9): 1001–1006. doi:10.1038/s41567-021-01290-4.

Coherent spin-wave transport in an antiferromagnet

J.R. Hortensius[#*,1], **D. Afanasiev**[#†,1], **M. Matthiesen**[1], **R. Leenders**[2], **R. Citro**[3], **A.V. Kimel**[4], **R.V. Mikhaylovskiy**[2], **B.A. Ivanov**[5], **A.D. Caviglia**[§,1]

[1]Kavli Institute of Nanoscience, Delft University of Technology, P.O. Box 5046, 2600 GA Delft, The Netherlands

[2]Department of Physics, Lancaster University, Bailrigg, Lancaster LA1 4YW, United Kingdom

[3]Dipartimento di Fisica “E.R. Caianiello”, Università di Salerno and Spin-CNR, I-84084 Fisciano (Sa), Italy

[4]Institute for Molecules and Materials, Radboud University Nijmegen, 6525 AJ Nijmegen, The Netherlands

[5]Institute of Magnetism, National Academy of Sciences and Ministry of Education and Science, 03142 Kyiv, Ukraine

[#] These authors contributed equally to this work.

Abstract

Magnonics is a research field complementary to spintronics, in which quanta of spin waves (magnons) replace electrons as information carriers, promising lower dissipation[1–3]. The development of ultrafast nanoscale magnonic logic circuits calls for new tools and materials to generate coherent spin waves with frequencies as high, and wavelengths as short, as possible[4,5]. Antiferromagnets can host spin waves at terahertz (THz) frequencies and are therefore seen as a future platform for the fastest and the least dissipative transfer of information[6–11]. However, the generation of short-wavelength coherent propagating magnons in antiferromagnets has so far remained elusive. Here we report the efficient emission and detection of a nanometer-scale wavepacket of coherent propagating magnons in antiferromagnetic $DyFeO_3$ using ultrashort pulses of light. The subwavelength confinement of the laser field due to large absorption creates a strongly non-uniform spin excitation profile, enabling the propagation of a broadband continuum of coherent THz spin waves. The wavepacket contains magnons with a shortest detected wavelength of 125 nm that propagate with supersonic velocities of more than 13 km/s into the

[*] j.r.hortensius@tudelft.nl . [†] dmytro.afanasiev@physik.uni-regensburg.de . [§] a.caviglia@tudelft.nl .

Author contributions:
D.A. and A.D.C. conceived the project. J.R.H., D.A. and M.M performed the experiments, analysed the data. B.A.I. developed the general theoretical framework describing the spin wave propagation. R.L and R.V.M. developed the theoretical formalism of the spin wave detection. B.A.I., R.C., R.V.M. and A.V.K. contributed to discussion and theoretical interpretation of the results. A.D.C. supervised the project. The manuscript was written by J.R.H., D.A. and A.D.C., with feedback and input from all co-authors.

Competing interests:
The authors declare no competing interests.

Europe PMC Funders Author Manuscripts

material. This source of coherent short-wavelength spin carriers opens up new prospects for THz antiferromagnetic magnonics and coherence-mediated logic devices at THz frequencies.

Antiferromagnetic insulators (AFMs) are prime candidates to replace ferromagnets (FMs) as active media in applications involving high-speed spin transport and large spectral bandwidth operation[6–8]. Integration of AFMs in future wave-based technologies[3] requires the realization of coherent (ballistic) transport of antiferromagnetic spin waves over large distances[5]. In this regard, non-uniform spin-wave modes with short wavelengths ($\lambda \lesssim$ 100 nm) are of particular importance: they can operate at THz clock rates, exhibit high propagation velocities and enable the miniaturization of devices down to the nanoscale. Phase-coherent ballistic spin transport in AFMs is also interesting from a fundamental point of view, as it is anticipated to be a prerequisite for the occurrence of exotic phenomena such as magnetic solitons[12], Bose-Einstein condensates[13,14] and spin-superfluidity[15–17]. Such prospects motivate a search for efficient methods for the excitation, manipulation, and detection of short-wavelength coherent antiferromagnetic magnons.

Conventional methods of linear spin-wave excitation use spatially varying oscillating magnetic fields. However, the high frequency of THz resonances inherent to antiferromagnetic dynamics make traditional field sources based on microstrip lines or coplanar waveguides impractical to be used in antiferromagnetic media. As a result, recent demonstrations of magnon-mediated spin transport in antiferromagnets were limited to either diffusive propagation of incoherent magnons[9–11] or evanescent spin-wave modes[18]. The experimental generation of coherent propagating short-wavelength magnons, which enables phase-coherent transport in an antiferromagnet, has so far not been achieved.

Ultrashort pulses of light have been routinely used to generate and to control large-amplitude THz spin precession[19–21] in antiferromagnets. The small photon momentum, however, poses a problem: it gives rise to a large momentum mismatch with short-wavelength spin waves. Consequently, optical techniques have so far been restricted to the generation of $k = 0$ uniform antiferromagnetic magnons and/or pairs of mutually coherent magnons at the edges of the Brillouin zone[22], for which group velocities are (near-)zero and no spatial transport of energy and angular momentum takes place. Here we overcome this problem and present an all-optical method to excite and detect a broadband wavepacket of short-wavelength coherent propagating magnons in an insulating antiferromagnet. Optical excitation of intense charge-transfer electronic transitions in the prototypical antiferromagnet $DyFeO_3$ with ultrashort pulses of light provides strong confinement of the light field, which creates a narrow exponential profile of deflected spins near the sample surface. This nanoscale magnetic non-uniformity serves as a source of short-wavelength coherent spin waves propagating into the sample bulk, as illustrated in Figure 1a. Using k-selective magneto-optical Bragg detection we map out spectral components of the magnon wavepacket and reveal magnon modes with nanoscale wavelengths, supersonic group velocities and an estimated propagation length of more than 1 μm.

Dysprosium orthoferrite ($DyFeO_3$) is a charge-transfer antiferromagnetic insulator with the Néel temperature $T_N = 645$ K, exhibiting one of the strongest observed interactions between spins and ultrashort laser pulses[19,23,24]. The optical spectrum of $DyFeO_3$ is dominated by a

Europe PMC Funders Author Manuscripts

set of intense electronic O-Fe (2*p*-3*d*) charge-transfer (CT) transitions. The absorption due to these transitions sets in above 2 eV, and promptly brings the absorption coefficient α to values as high as 5×10^5 cm^{-1} (see inset Fig. 1a)[25], corresponding to penetration depths (δ) of less than 50 nm.

In our experiments we study a 60 μm thick slab of *z*-cut $DyFeO_3$. The sample is excited with 100 fs pump pulses which have photon energy tunable in the spectral range of 1.5 – 3.1 eV, covering the lowest energy $^6A_{1g} \rightarrow {}^6T_{1u}$ charge-transfer electronic transition[25]. We use time-delayed probe pulses at various photon energies below the charge-transfer gap ($h\nu < 2$ eV) to detect the photo-induced magnetic dynamics, see Extended Data Fig. 1. The probing is performed simultaneously in the two complementary transmission and reflection geometries (see Fig. 1b). In both geometries, the pump-induced rotation of the probe polarization plane, originating from the Faraday effect (θ_F) or the magneto-optical Kerr effect (MOKE) (θ_K), is tracked as a function of the pump-probe time delay. Note that while the Faraday transmission geometry is routinely used in pump-probe experiments for detecting uniform ($k = 0$) spin precession in antiferromagnets[19], the reflection geometry has been shown to enable detection of finite-*k* coherent excitations such as propagating acoustic wavefronts[26,27]. As shown below we demonstrate that the reflection geometry can be also used to probe the dynamics of short-wavelength propagating coherent spin waves.

Following the optical pumping in the regime of strong absorption ($h\nu = 3.1$ eV) the time-resolved dynamics reveal high-frequency oscillations in the hundreds of GHz range (see Fig. 1c). The frequencies f_0 and f_k of the oscillations observed in the transmission and reflection geometry respectively, are substantially different: $f_k > f_0$ (see inset Fig. 1c). The decay time of the oscillations also differs by nearly an order of magnitude.

To identify the origin of the oscillations, we track their central frequency as a function of temperature. The antiferromagnetic state in $DyFeO_3$ adopts two distinct spin configurations, sharply separated by a first-order phase transition at the so-called Morin temperature $T_M \backsimeq 50$ K[28]. At $T < T_M$, the antiparallel iron spins are oriented along the *y*-axis and arranged in a compensated collinear AFM pattern. Above T_M, the spins experience a reorientation towards the *x*-axis accompanied by the mutual canting and stabilization of a canted AFM phase (see Fig. 2a). The temperature dependence of the oscillation frequency exhibits a characteristic cusp-like softening with a minimum at T_M (see Fig. 2b and Extended Data Fig. 2). This frequency softening is a hallmark of the quasi-antiferromagnetic (*q*-AFM) magnon branch in $DyFeO_3$ and is caused by strong temperature variations of the magneto-crystalline anisotropy in the vicinity of T_M [29]. Indeed, the frequencies f_0 observed in the transmission geometry match values reported in literature for the zone-centre ($k = 0$) *q*-AFM magnon[29].

To explain the physical origin of the oscillation at frequency f_k seen in the MOKE experiment, we refer to the dispersion relation for magnons. In both magnetic phases, below and above T_M, the magnon spectrum ω_k in $DyFeO_3$, is given by[30]:

$$\omega_k = \sqrt{\omega_0^2 + (v_0 k)^2} \quad (1)$$

where $v_0 \approx 20$ km/s is the limiting group velocity of the spin waves[30]. This dispersion relation is shown as an inset to Fig. 2b. At small wavenumbers $kv_0 \ll \omega_0$, it has a quadratic form due to the magnon gap $\omega_0 = 2\pi f_0$, arising from magneto-crystalline anisotropy. At larger wavenumbers $v_0 k \gg \omega_0$, the dispersion relation becomes dominated by the exchange interaction (exchange regime), and thus takes a linear form typical for antiferomagnets[30]. Based on the form and properties of the dispersion relation we identify the MOKE signal at f_k as a finite-k magnon on the q-AFM branch: it follows the characteristic temperature dependence of the f_0 zone-center magnon mode and has a nearly temperature-independent blueshift. The detection geometry implies that the magnon wavevector **k** is perpendicular to the sample surface, and its magnitude can be deduced from Eq. (1) to be $k = 4.2\times10^5$ cm^{-1} ($\lambda = 2\pi/k \approx 140$ nm, see Figure 2b).

By considering the modulation of the material's dielectric tensor due to the propagating coherent spin waves, we can further support the attribution of the f_k oscillation to a finite-k magnon on the q-AFM branch. A spin wave with a propagation vector along the z-axis causes a perturbation of the magnetic order and a corresponding periodic modulation of the off-diagonal components of the dielectric tensor[31], resembling the magneto-optical analogue of a dynamical volume phase grating. The polarization state of the reflected probe is explained by the Bragg reflection of light from this grating, an approach similar to the one used in Brillouin light scattering studies on spin waves[32]. As a result, the polarization rotation of the reflected probe beam with wavenumber k_0 becomes subject to a Bragg condition:

$$k_{\mathrm{m}} = 2k_0 n(\lambda_0)\cos\gamma' \tag{2}$$

where $n(\lambda_0)$ is the optical refractive index of the medium at the probe wavelength λ_0, γ' is the refracted angle of incidence of the probe, and k_{m} is the normal projection of the **k**-vector of the probed magnon (see Supplementary section S1). Using Eq. (2) we find that a probe pulse at a central wavelength of 680 nm ($n \approx 2.39$)[25] and normal incidence ($\gamma' = 0$) is sensitive to propagating magnons with wavenumber $k_{\mathrm{m}} \approx 4.2\times10^5$ cm^{-1}. Note that this independent estimation agrees with the magnon wavenumber retrieved using the measured frequency and the known dispersion relation (Eq. (1)).

The generation of finite-k coherent magnons is anticipated to rely strongly on the confinement provided by the optical penetration depth δ, which is highly dispersive near the charge-transfer band. In particular, changing the pump photon energy between 2.4 eV and 3.1 eV provides a variation in the penetration depth between 300 and 50 nm, while the real part of the refractive index (influencing the pump wavelength) changes by only 5% (see Extended Data Fig. 3). Therefore, the amplitude of the finite-k magnon is expected to vary strongly as function of the pump photon energy. The time-resolved MOKE signals obtained in the reflection geometry for different photon energies of the pump excitation, are shown in Fig. 3a. The Fourier transforms of the signals (Fig. 3b) show that the spectra are composed of two components, corresponding to the zone-centre and finite-k ($k_{\mathrm{m}} = 3.7\times10^5$ cm^{-1}) magnon modes. One can see that with increasing photon energy (i.e. decreasing penetration depth), the amplitude of the finite-k magnon mode increases dramatically (see Fig. 3c). The obtained dependence shows that the finite-k magnon is nearly absent for penetration depths

larger than 150 nm, a value close to the wavelength λ_m of the probed magnons, and grows dramatically for shorter penetration depths.

We model this observation using a simple assumption: the ultrashort light pulse promotes a spin excitation that is strongly non-uniform along the direction of incidence *z*. The excitation leads to a nearly instantaneous deflection of spins by an angle $\varphi(z)$ with the spatial distribution following the optical absorption profile given by the Beer-Lambert law: $\varphi(z, t = 0) = \varphi_0 e^{-z/\delta}$, where $\varphi_0 \sim I_0/\delta$ is proportional to the intensity of the pump pulse I_0, and inversely proportional to the light penetration depth (see Supplementary section S2). The strongly non-uniform spin perturbation distributes the initial deflection among magnon modes at different *k*-wavenumbers, with the amplitudes A_k given by the reciprocal space image of the initial excitation (see inset Fig. 3c):

$$A_k \sim \frac{I_0}{1 + (k\delta)^2} \tag{3}$$

This expression not only agrees well with the observations of Fig. 3c ($k_m \approx 3.7\times10^5$ cm^{-1}, λ_m = 170 nm), where it is plotted as a best fit to the pump intensity I_0, but also confirms the intuitive interpretation that a stronger confinement shifts the spectral amplitude of the excited magnon wave packet towards larger *k*.

The excited spin-wave continuum forms a broadband magnon wavepacket, in which individual spectral components propagate independently, each adhering to the dispersion relation $\omega_k = 2\pi f_k$ (Eq. (1)). In order to visualize the time evolution of the wavepacket, we make use of the linearized sine-Gordon equation for the space- (z) and time- (t) dependent amplitude of the spin deflections $\varphi(z,t)$[30] (see Supplementary section S2). The evolution of the spin dynamics is described by:

$$\varphi(z, t) = \frac{2}{\pi} \int_{-\infty}^{\infty} \mathrm{d}k \left[A_k \cos(kz) \cos(\omega_k t) \right] \tag{4}$$

and is shown in Fig. 4a and Extended Data Fig. 4. The strong dispersion promptly smears out the initial exponential profile of the spin excitation, simultaneously forming a spin-wave front that propagates into the bulk, already after around 10 ps. This front is composed of short-wavelength magnons with $k \gtrsim 20\times10^5$ cm^{-1} propagating with the limiting group velocity v_0.

Applying the Bragg condition of Eq. (2), we can experimentally map out the spectral components of the magnon wavepacket, as well as extract the group velocity and propagation length of individual magnon modes. First, we vary the incidence angle γ of the probe pulse, (inset Fig. 4b) and find that the central frequency of the oscillations is reduced upon increasing γ' (Fig. 4b), in perfect agreement with Eq. (2) and the magnon dispersion of Eq. (1). Next, upon decreasing the probe wavelength, we observe a systematic increase in the magnon frequency (Fig. 4c), once again in accordance with the Bragg condition.

To summarize our observations, we plot the extracted central frequencies as a function of the corresponding wavenumbers k_{m} (see Fig. 4d). These points, fit to the dispersion relation ω_k given by Eq. (1), yield a limiting group velocity $v_0 = 19.7 \pm 0.1$ km/s, in good agreement with the literature values[30]. Using this extracted value, we evaluate the group velocities $v_{\mathrm{g}} = \left.\frac{\partial \omega_k}{\partial k}\right|_{k = k_m}$ of the optically detected magnons given by $v_{\mathrm{g}} = v_0^2 \frac{k_{\mathrm{m}}}{\omega_k}$. These values, shown in Fig. 4e, indicate that while the zone-center magnons do not support propagation, the shortest-wavelength components of the magnon wavepacket detected in our experiment propagate at a supersonic ($v_s = 6$ km/s, see Supplementary Section S3) velocity of nearly 13 km/s. We note that these magnons already approach the exchange wave regime characterized by the limiting group velocity v_0. This feature, inherent to antiferromagnets, stands in contrast with the situation in ferromagnets, where the quadratic dispersion relation dictates that the exchange value of the group velocity is reached only for magnons with $\lambda \lesssim 10$ nm. Although the shortest magnon wavelength detected in our experiments is 125 nm, magnons at even shorter wavelengths, down to the penetration depth limit of 50 nm, are anticipated, and could be detected using probe pulses at higher photon energies or other means to measure non-local ultrafast spin excitations[33–35]. Using the extracted lifetime of the oscillations $\tau = 85$ ps (see Extended Data Fig. 5), we estimate the coherence length l_{c} of the spin-wave transport $l_{\mathrm{c}} = v_{\mathrm{g}}\, \tau = 1.1$ μm. We note that this length, enhanced as compared to metallic antiferromagnets[8,36], also agrees with studies of diffusive spin transport in other insulating antiferromagnets[9,37]. One can anticipate even longer propagation lengths for the coherent (ballistic) regime reported here: our estimate of the coherence length is only a lower limit, as the propagating spin wave is likely to escape from the region that is probed by the reflected probe light (of the order of $\lambda_0/2$). These observations make antiferromagnetic insulators such as $DyFeO_3$ a promising platform for the realization of high-speed wave-based magnonic devices.

Through optical pumping of above-bandgap electronic transitions, we have explored an efficient and virtually universal route for exciting coherent propagating spin waves in insulating antiferromagnets. The strong optical absorption provides an opportunity to spatially confine the light to a subwavelength scale, inaccessible by any other means, such as for example focusing[38–40], enabling the emission of a broadband continuum of short-wavelength antiferromagnetic magnons. The universal mechanism opens up prospects for terahertz coherent AFM magnonics and opto-spintronics[7] providing a long-sought source of coherent high-velocity spin waves. We anticipate even higher propagation velocities to be observed in the broad class of easy-plane antiferromagnets (e.g. hematite[37] and $FeBO_3$), in which the spin-wave gap ω_0 is reduced and the high-velocity exchange wave regime can be achieved at significantly smaller wavenumbers k. The demonstrated approach holds promise for a wide range of fundamental studies exploiting the excitation and propagation of non-linear spin waves such as magnetic solitons[12,41] as well as the investigation of the giant magneto-elastic coupling between antiferromagnetic magnons and acoustic phonons[42] directly in the time domain.

Methods

Sample

A single crystal of $DyFeO_3$, 60 μm thick, grown by a floating zone melting technique was used in this work. The sample is cut perpendicularly to the crystallographic *z*-axis.

Time-resolved experiment

The experimental setup is schematically shown in Extended Data Figure 1.

An amplified 1 kHz Ti:Sapphire laser system (Astrella, Coherent, central wavelength 800 nm, pulse energy: 7 mJ, pulse duration: 100 fs) forms the basis of the experimental setup. A large fraction of this output is used to pump a dual optical parametric amplifier (OPA, TOPAS-Twins, Light Conversion). The OPA delivers linearly polarized, 100 fs output pulses, with photon energies $h\nu$ in the range 0.45–1 eV (λ_0 = 2.7–1.4 μm). The photon energy of these output pulses was doubled or tripled using a β-barium borate (BBO) single crystal in order to obtain tunable excitation pulses which cover the photon energies in the optical range of 1.55–3.1 eV (corresponding wavelength 400–800 nm). A small portion of the amplifier pulses was sent through a mechanical delay line and used as probe of the spin dynamics in the reflection and transmission geometries.

Pump and probe pulse were focused onto the $DyFeO_3$ sample (pump spot diameter: 300 μm, typical fluence 2 mJ/cm^2, probe spot diameter: 80 μm), which was kept in a dry-cycle cryostat (Montana Instruments) that allowed to cool it down to 10 K and vary the temperature with high stability in a wide temperature range (10–250 K). The pump-induced changes in the polarization $\theta_{K,F}$ of the reflected or transmitted probe pulse were measured using an optical polarization bridge (Wollaston prism) and a pair of balanced Si photodetectors.

Experimental determination of the absorption coefficient

The unpolarised absorption spectrum of $DyFeO_3$ was directly obtained with light propagating along the crystal *z*-axis in the spectral region 1–2.2 eV. The resulting absorption is shown in the inset of Figure 1a. In addition, we performed spectroscopic ellipsometry measurements using a Woollam M5000 ellipsometer over a wide energy range to obtain the real and imaginary parts of the refractive index. In the photon energy region 2.5–4 eV, where the transmission measurements are not possible for thick samples, we estimated the absorption using the acquired complex refractive index. These values are shown in the inset of Figure 1a.

Europe PMC Funders Author Manuscripts

Extended Data

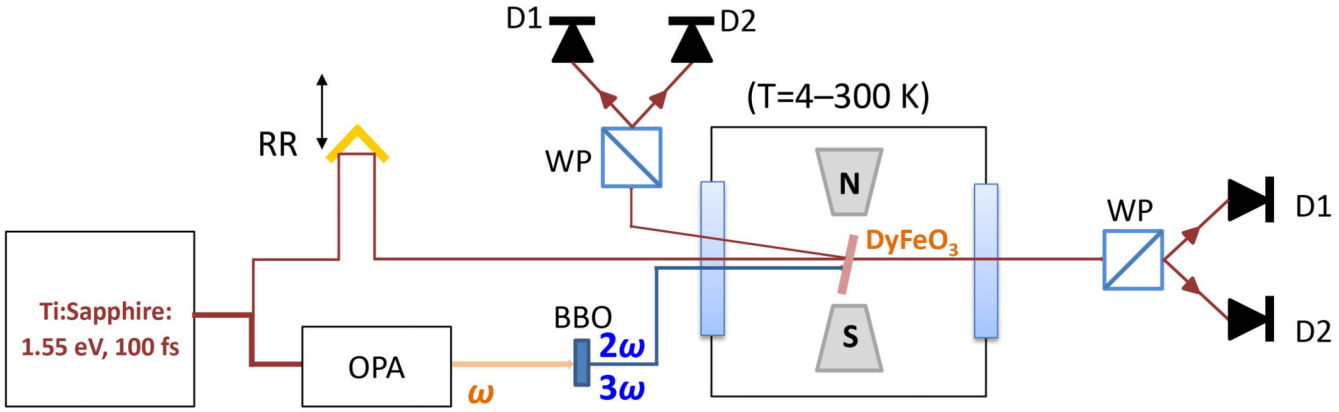

Extended Data Fig. 1. Experimental setup

RR: gold retroreflector mounted on a motorized precision delay stage, OPA: optical parametric amplifier, BBO: β-barium borate crystal, WP: Wollaston Prism, D1, D2: a pair of balanced silicon photodetectors.

Europe PMC Funders Author Manuscripts

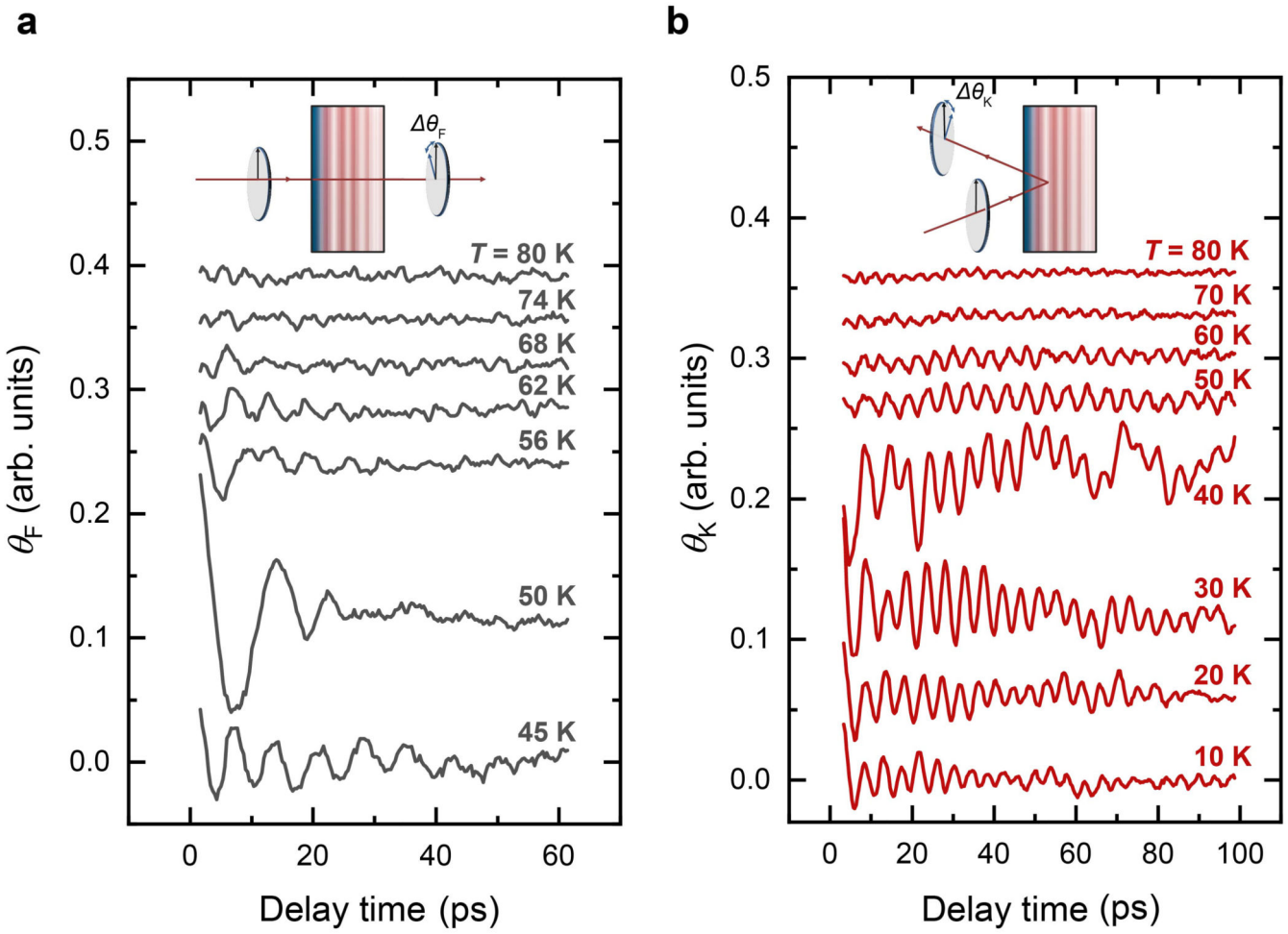

Extended Data Fig. 2. Time-resolved spin-wave detection at different temperatures

(**a,b**) Time resolved polarization rotation in the transmission (a) and reflection geometry (b) following excitation at $h\nu$ = 3.1 eV for different temperatures. The probe incidence angle is near-normal, with λ_0 = 700 nm.

Europe PMC Funders Author Manuscripts

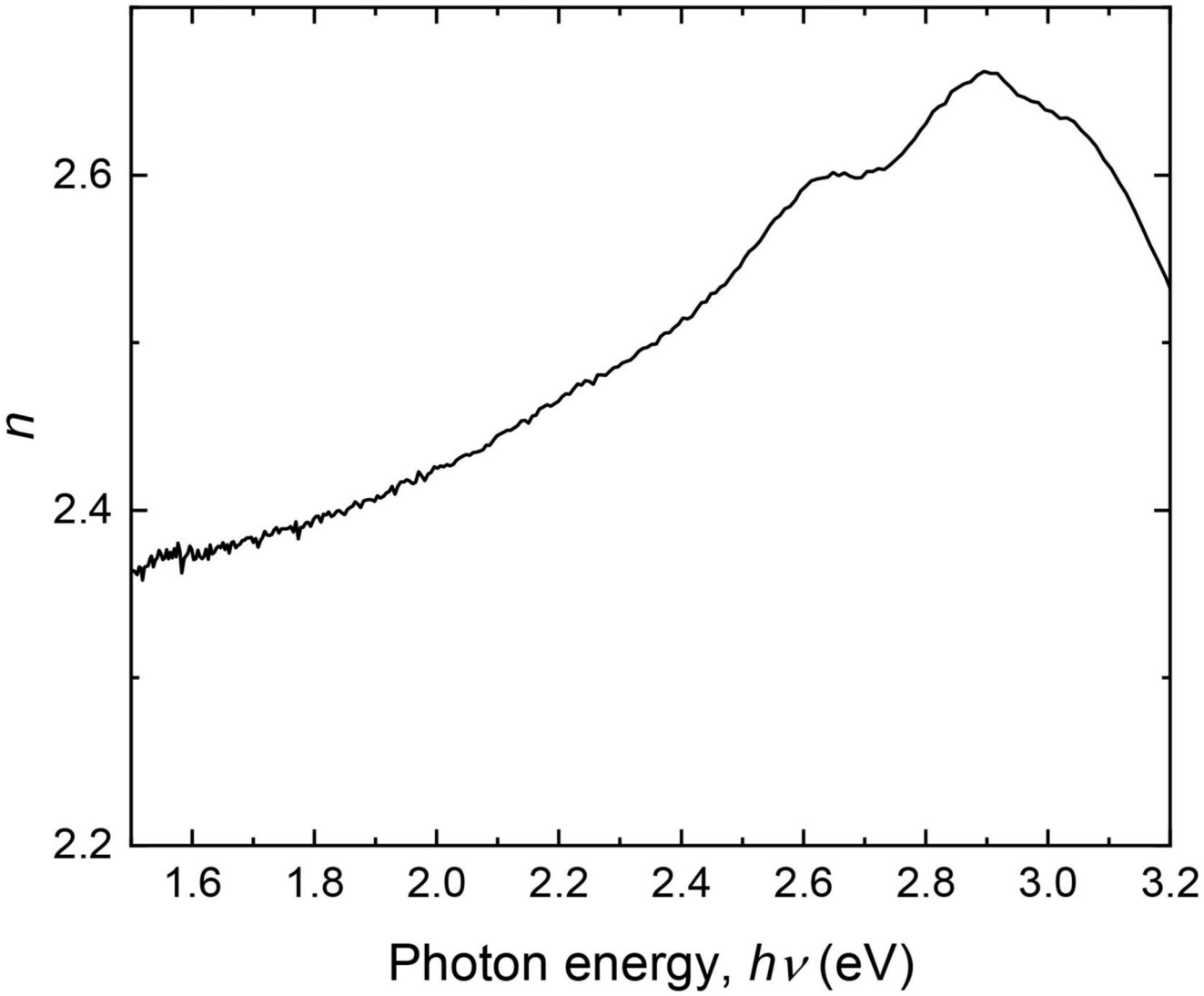

Extended Data Fig. 3. Real part of the refractive index as a function of the pump photon energy

Real part n of the refractive index, as extracted using spectroscopic ellipsometry measurements.

Europe PMC Funders Author Manuscripts

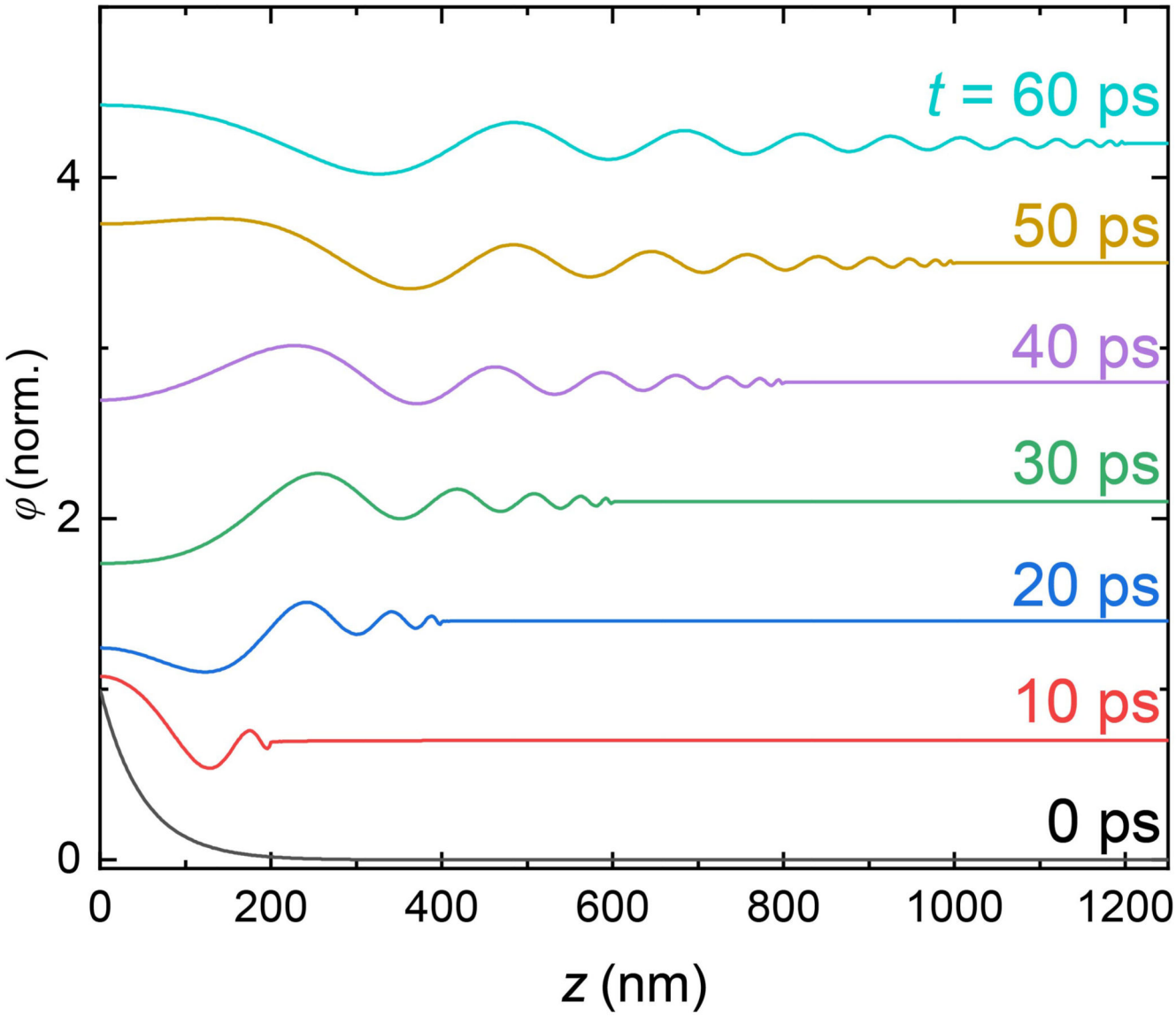

Extended Data Fig. 4. Simulations of the light-induced spin wave dynamics

Real-space distribution of the magnon spin deflection at different times *t*, after optical excitation at $h\nu$ = 3.1 eV with a penetration depth of 50 nm, as determined by Eq. (3).

Europe PMC Funders Author Manuscripts

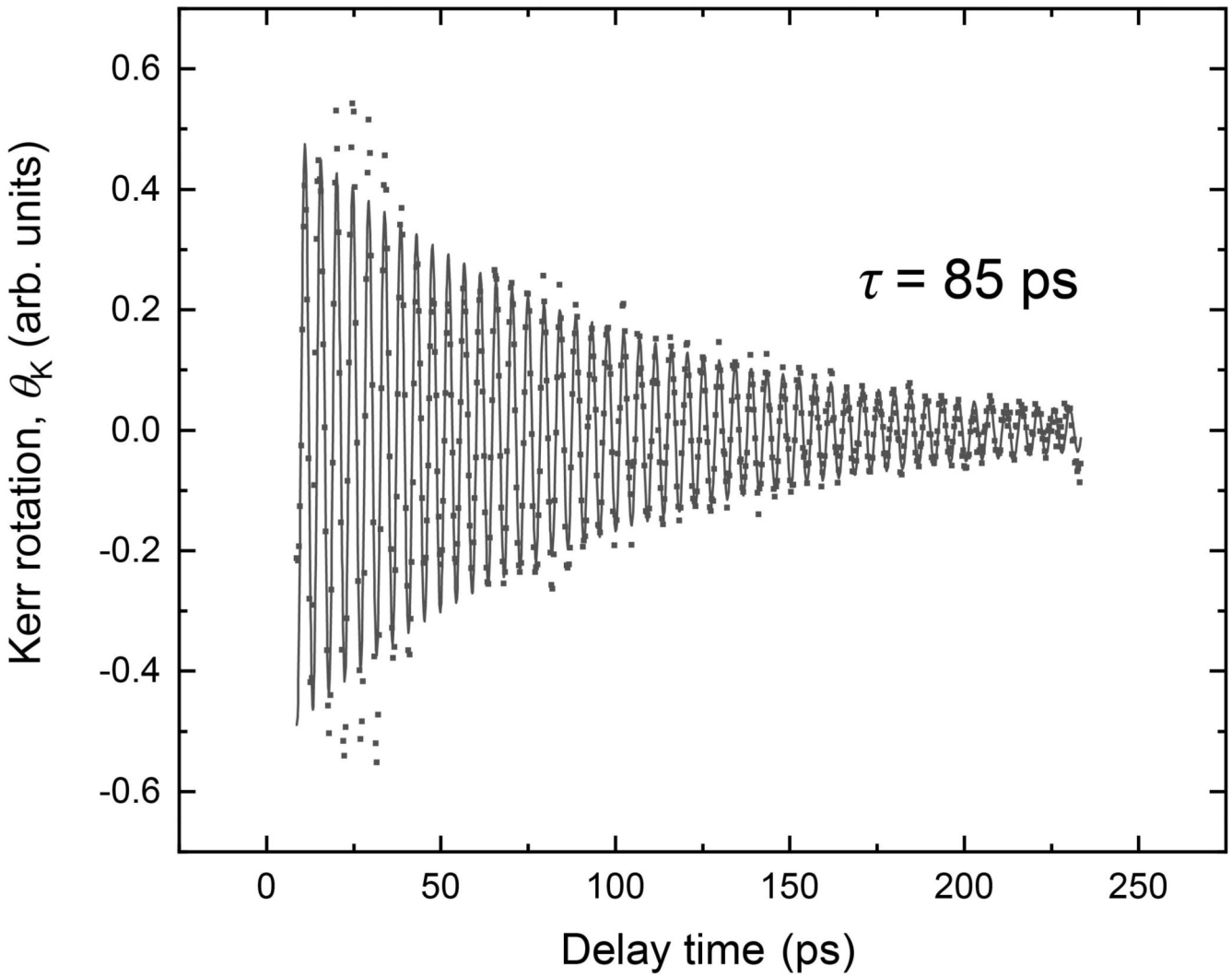

Extended Data Fig. 5. Extracting the magnon propagation distance

Time-resolved polarization rotation originating from a propagating magnon, as obtained in the reflection geometry. The solid line represents a best fit of a damped sine, giving a lifetime of about 85 ps. With the largest estimated group velocities vg of the measured magnons of about 13 km/s, this gives a propagation distance $l_c = v_g\tau = 1.1$ μm.

Supplementary Material

Refer to Web version on PubMed Central for supplementary material.

Acknowledgements

The authors thank V.V. Kruglyak and R. Rejali for critically reading the manuscript and T.C. van Thiel and E. Demler for useful discussions. This work was supported by the EU through the European Research Council, Grant No. 677458 (AlterMateria), the Netherlands Organization for Scientific Research (NWO/OCW) as part of the Frontiers of Nanoscience program (NanoFront) and the VENI-VIDI-VICI program. R.V.M and R.L. acknowledge support from the European Research council, Grant No. 852050 (MAGSHAKE). R.C. acknowledges support by the project Quantox, Grant No. 731473, QuantERA-NET Cofund in Quantum Technologies, implemented within

the EU-H2020 Programme. B.A.I acknowledges support from the National Scientific Foundation of Ukraine under Grant. No. 2020.02/0261.

Data Availability

Source data for figures are publicly available with identifier (DOI) 10.5281/zenodo.4716539. All other data that support the findings of this paper are available from the corresponding author upon request.

Code Availability

The code used to simulate the magnon dynamics is available upon reasonable request.

References

1. Kruglyak VV, Hicken RJ. Magnonics: Experiment to prove the concept. J Magn Magn Mater. 2006; 306 :191–194.
2. Kruglyak VV, Demokritov S, Grundler D. Magnonics. J Phys D. 2010; 43 264001
3. Lenk B, Ulrichs H, Garbs F, Münzenberg M. The building blocks of magnonics. Phys Rep. 2011; 507 :107–136.
4. Chumak AV, Vasyuchka VI, Serga AA, Hillebrands B. Magnon spintronics. Nat Phys. 2015; 11 :453–461.
5. Sander D, et al. The 2017 magnetism roadmap. J Phys D. 2017; 50 363001
6. Jungwirth T, Marti X, Wadley P, Wunderlich J. Antiferromagnetic spintronics. Nat Nanotechnol. 2016; 11 :231–241. [PubMed: 26936817]
7. Nemec P, Fiebig M, Kampfrath T, Kimel AV. Antiferromagnetic opto-spintronics. Nat Phys. 2018; 14 :229–241.
8. Baltz V, et al. Antiferromagnetic spintronics. Rev Mod Phys. 2018; 90 015005
9. Lebrun R, et al. Tunable long-distance spin transport in a crystalline antiferromagnetic iron oxide. Nature. 2018; 561 :222–225. [PubMed: 30209370]
10. Li J, et al. Spin current from sub-terahertz-generated antiferromagnetic magnons. Nature. 2020; 578 :70–74. [PubMed: 31988510]
11. Vaidya P, et al. Subterahertz spin pumping from an insulating antiferromagnet. Science. 2020; 368 :160–165. [PubMed: 32273462]
12. Galkina E, Ivanov B. Dynamic solitons in antiferromagnets. Low Temp Phys. 2018; 44 :618–633.
13. Giamarchi T, Rüegg C, Tchernyshyov O. Bose–Einstein condensation in magnetic insulators. Nat Phys. 2008; 4 :198–204.
14. Johansen Ø, Kamra A, Ulloa C, Brataas A, Duine RA. Magnon-mediated indirect exciton condensation through antiferromagnetic insulators. Phys Rev Lett. 2019; 123 167203 [PubMed: 31702374]
15. Bunkov YM, et al. High-T_c spin superfluidity in antiferromagnets. Phys Rev Lett. 2012; 108 177002 [PubMed: 22680894]
16. Takei S, Halperin BI, Yacoby A, Tserkovnyak Y. Superfluid spin transport through antiferromagnetic insulators. Phys Rev B. 2014; 90 094408
17. Qaiumzadeh A, Skarsvåg H, Holmqvist C, Brataas A. Spin superfluidity in biaxial antiferromagnetic insulators. Phys Rev Lett. 2017; 118 137201 [PubMed: 28409991]
18. Dąbrowski M, et al. Coherent transfer of spin angular momentum by evanescent spin waves within antiferromagnetic NiO. Phys Rev Lett. 2020; 124 217201 [PubMed: 32530697]
19. Kimel A, et al. Ultrafast non-thermal control of magnetization by instantaneous photomagnetic pulses. Nature. 2005; 435 :655–657. [PubMed: 15917826]
20. Duong N, Satoh T, Fiebig M. Ultrafast manipulation of antiferromagnetism of NiO. Phys Rev Lett. 2004; 93 117402 [PubMed: 15447379]

21. Kampfrath T, et al. Coherent terahertz control of antiferromagnetic spin waves. Nat Photonics. 2011; 5 :31–34.
22. Bossini D, et al. Macrospin dynamics in antiferromagnets triggered by sub-20 femtosecond injection of nanomagnons. Nat Commun. 2016; 7 10645 [PubMed: 26847766]
23. Afanasiev D, et al. Ultrafast control of magnetic interactions via light-driven phonons. Nat Mater. 2021; 20 :607–611. [PubMed: 33558717]
24. Afanasiev D, et al. Control of the ultrafast photoinduced magnetization across the Morin transition in $DyFeO_3$. Phys Rev Lett. 2016; 116 097401 [PubMed: 26991201]
25. Usachev P, et al. Optical properties of thulium orthoferrite $TmFeO_3$. Phys Solid State. 2005; 47 :2292–2298.
26. Thomsen C, Grahn HT, Maris HJ, Tauc J. Surface generation and detection of phonons by picosecond light pulses. Phys Rev B. 1986; 34 :4129–4138.
27. Hortensius JR, Afanasiev D, Sasani A, Bousquet E, Caviglia AD. Ultrafast strain engineering and coherent structural dynamics from resonantly driven optical phonons in $LaAlO_3$. npj Quantum Mater. 2020; 5 :95.
28. Afanasiev D, Zvezdin A, Kimel A. Laser-induced shift of the Morin point in antiferromagnetic $DyFeO_3$. Opt Express. 2015; 23 :23978–23984. [PubMed: 26368488]
29. Balbashov A, Volkov A, Lebedev S, Mukhin A, Prokhorov A. High-frequency magnetic properties of dysprosium orthoferrite. Zh Eksp Teor Fiz [Sov Phys JETP]. 1985; 88 :974–987.
30. Bar'yakhtar VG, Ivanov B, Chetkin MV. Dynamics of domain walls in weak ferromagnets. Sov Phys Usp. 1985; 28 :563–588.
31. Zvezdin, AK, Kotov, VA. Modern magnetooptics and magnetooptical materials. CRC Press; 1997.
32. Demokritov SO, Hillebrands B, Slavin AN. Brillouin light scattering studies of confined spin waves: linear and nonlinear confinement. Phys Rep. 2001; 348 :441–489.
33. Qiu H, et al. Ultrafast spin current generated from an antiferromagnet. Nat Phys. 2021; 17 :388–394.
34. Razdolski I, et al. Nanoscale interface confinement of ultrafast spin transfer torque driving non-uniform spin dynamics. Nat Commun. 2017; 8 15007 [PubMed: 28406144]
35. Melnikov A, et al. Ultrafast transport of laser-excited spin-polarized carriers in Au/Fe/MgO (001). Phys Rev Lett. 2011; 107 076601 [PubMed: 21902412]
36. Siddiqui SA, et al. Metallic antiferromagnets. J Appl Phys. 2020; 128 040904
37. Lebrun R, et al. Long-distance spin-transport across the Morin phase transition up to room temperature in the ultra-low damping single crystals of the antiferromagnet α-Fe_2O_3 . Nat Commun. 2020; 11 6332 [PubMed: 33303758]
38. Hashimoto Y, et al. All-optical observation and reconstruction of spin wave dispersion. Nat Commun. 2017; 8 15859 [PubMed: 28604690]
39. Satoh T, et al. Directional control of spin-wave emission by spatially shaped light. Nat Photonics. 2012; 6 :662–666.
40. Au Y, et al. Direct excitation of propagating spin waves by focused ultrashort optical pulses. Phys Rev Lett. 2013; 110 097201 [PubMed: 23496741]
41. Bonetti S, et al. Direct observation and imaging of a spin-wave soliton with *p*-like symmetry. Nat Commun. 2015; 6 8889 [PubMed: 26567699]
42. Ozhogin V, Preobrazhenskiĭ V. Anharmonicity of mixed modes and giant acoustic nonlinearity of antiferromagnetics. Sov Phys Usp. 1988; 31 :713–729.

Europe PMC Funders Author Manuscripts

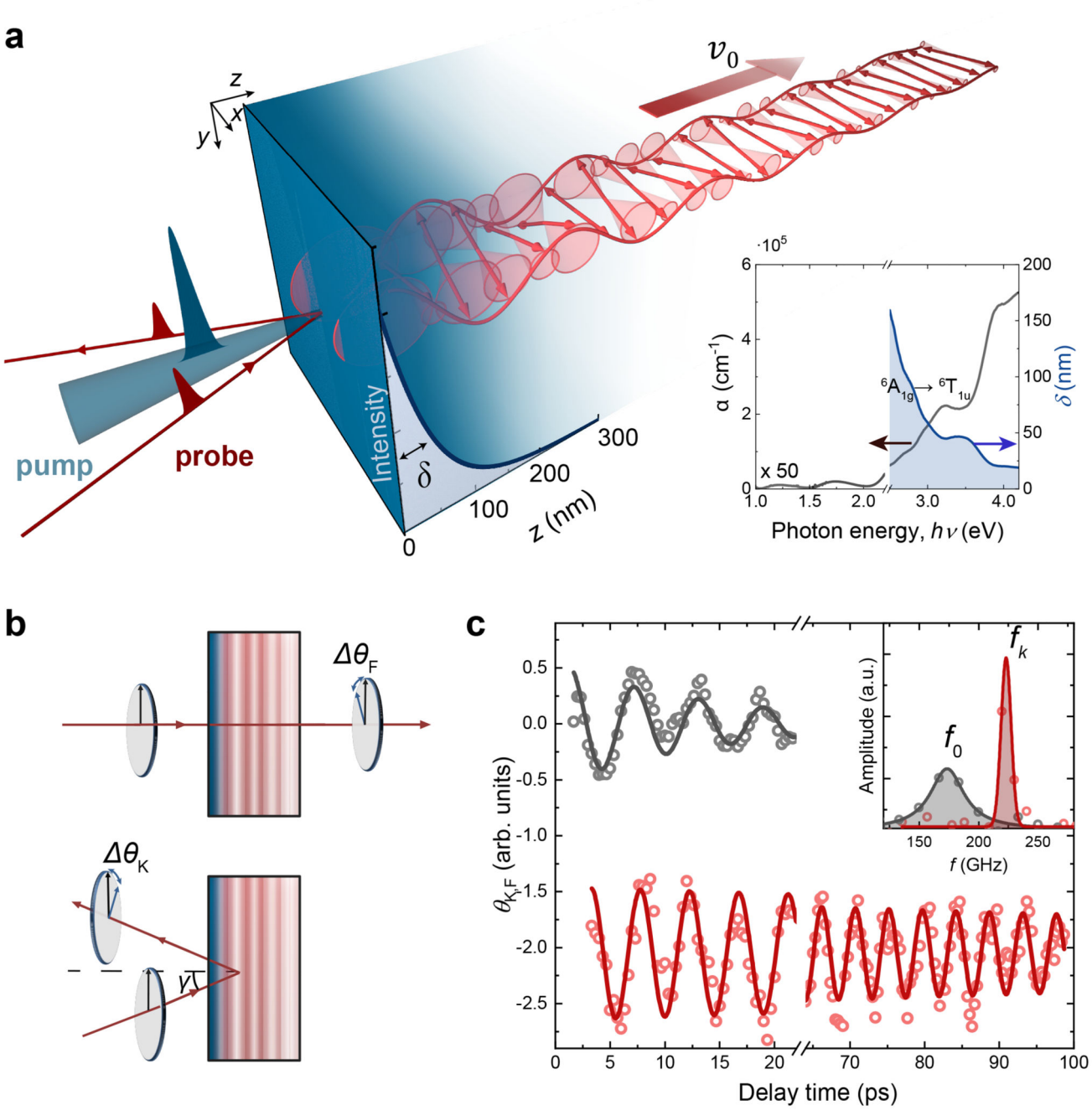

Figure 1. All-optical generation and detection of coherent antiferromagnetic spin waves.

(**a**) Schematic illustration of the generation of propagating antiferromagnetic spin waves after optical excitation of strongly absorbing electronic transitions. The optical penetration depth δ of the light defines the excited region and the width of the magnetic non-uniformity. Inset: Absorption coefficient α (left axis) and corresponding penetration depth δ (right axis) for $DyFeO_3$ as function of photon energy $h\nu$ (see Methods). $^6A_{1g} \rightarrow {}^6T_{1u}$: the charge-transfer transition of interest. (**b**) Schematics for the optical detection mechanisms of spin waves in transmission (top) and reflection (bottom) geometries, measuring transient

changes in the Faraday rotation (θ_F) and Kerr rotation (θ_K) respectively; γ is the angle of incidence. (**c**) Time-resolved measurements of the polarization rotation of a near-infrared probe pulse after excitation with pump pulses with a photon energy of 3.1 eV (δ = 50 nm) in the detection geometries shown in (b): (top) transmission, (bottom) reflection. The thick solid lines are exponentially damped sine fits. Inset: Fourier spectra of the oscillations with Lorentzian fits (thick solid lines), with central frequencies f_0 (transmission geometry) and f_k (reflection geometry). a.u.: arbitrary units.

Europe PMC Funders Author Manuscripts

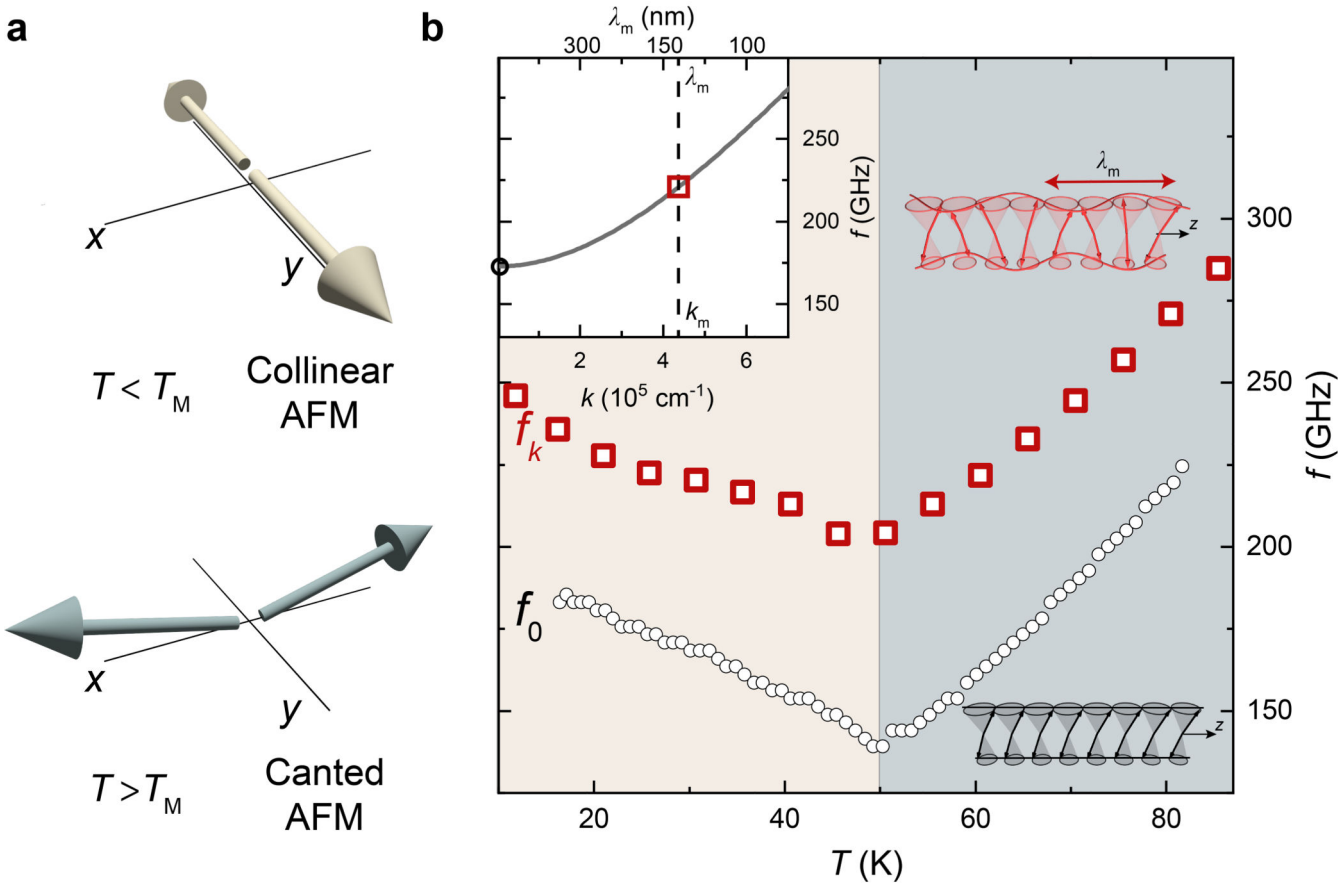

Figure 2. Temperature evolution of the spin-wave frequencies.

(**a**) The orientation of iron spins in the collinear AFM (top panel) and canted AFM phase (bottom panel). (**b**) Temperature (T) dependence of the central frequency of the oscillatory dynamics as measured in the reflection geometry (f_k, red square markers) compared with the $k = 0$ magnon T-dependence, as measured in transmission geometry (f_0, black circle markers). The pump photon energy $h\nu = 3.1$ eV. See also Extended Data Fig. 2. Left top inset: The antiferromagnetic magnon dispersion of $DyFeO_3$. Right insets: Schematic illustration of the spin wave corresponding to the oscillatory dynamics at the different frequencies.

Europe PMC Funders Author Manuscripts

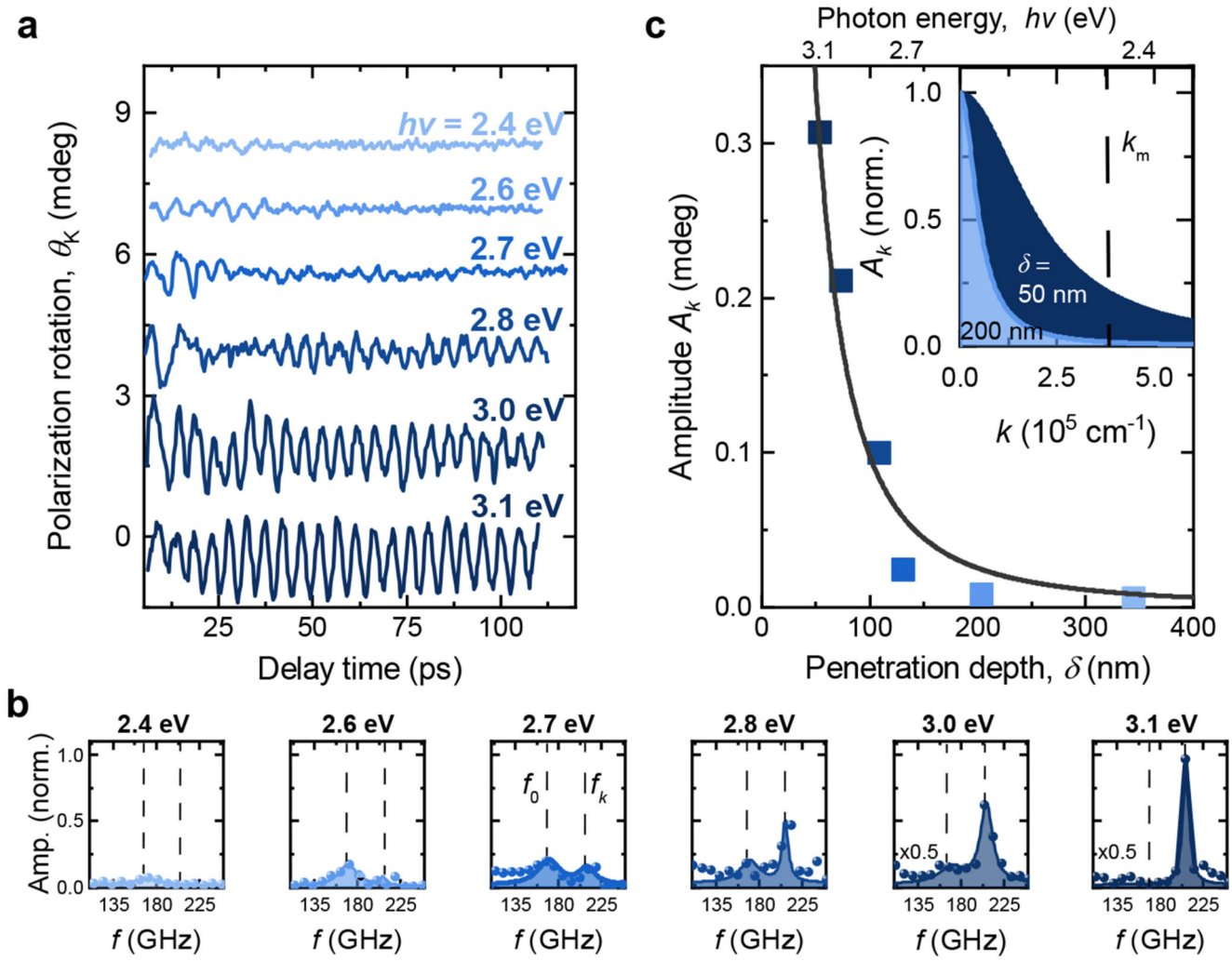

Figure 3. Confinement of the light as a necessary condition for the generation of finite-*k* spin waves.

(**a**) Time-resolved signals of the polarization rotation of the near-infrared probe pulse after excitation with pump pulses with increasing photon energy as measured in the reflection geometry. (**b**) Fourier amplitude spectra of the time-resolved signals from panel (a). (**c**) Amplitude of sine fit oscillations corresponding to the AFM propagating spin wave to the data from panel (a) vs. penetration depth of the excitation pulse (color markers correspond to traces in panel (a)). The solid line is a theory fit using Eq. (3). Inset: Magnon frequency distribution after excitation with pump pulses with $\delta = 50$ nm (dark blue, broadband distribution) and 200 nm (light blue, narrowband). The probe is sensitive to $k_m = 3.7\times10^5$ cm^{-1}, indicated by the dashed line.

Europe PMC Funders Author Manuscripts

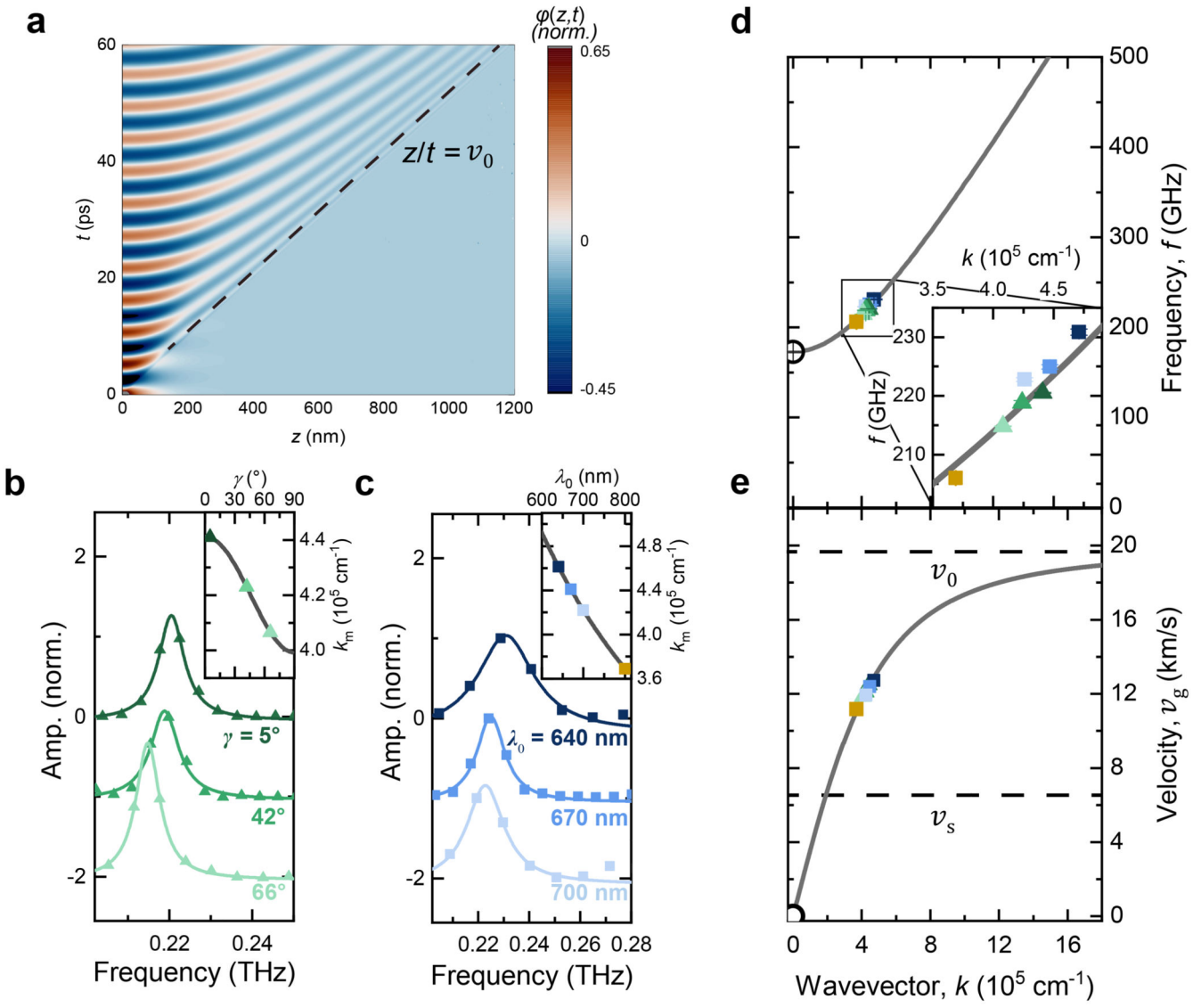

Figure 4. Revealing spectral components of the broadband antiferromagnetic magnon wavepacket.

(**a**) Simulation of the time- and position-dependent spin deflection $\varphi(z,t)$ after optical excitation at 3.1 eV with a penetration depth of 50 nm, as determined by Eq. (4). (**b,c**) Fourier spectra of time-resolved measurements of the polarization rotation of a near-infrared probe pulse obtained in the reflection geometry after excitation with pump pulses with a photon energy of 3.1 eV at the temperature T = 60 K for different probe incidence angles γ (λ_0 = 680 nm) (a) and probe wavelengths λ_0 (γ = 5°) (b). The solid superimposed lines are Lorentzian fits of the Fourier peaks. Insets: The wavenumber k_m of the probed magnons, as a function of the angle γ (b) and probe wavelength λ_0 (c), with the measured points indicated by coloured markers. (**d,e**) The extracted central magnon frequencies (d) and the calculated group velocity (e) from the data in panel (b) and (c) at their respective calculated wavenumbers plotted with a best fit of the spin-wave dispersion curve (d) and the group

velocity corresponding to the dispersion(e). The marker colours and shapes correspond to the measurements in panel (b) and (c).

Europe PMC Funders Author Manuscripts